

Inverse modelling of CF₄ and NF₃ emissions in East Asia

Tim Arnold^{1,2,3*}, Alistair J. Manning³, Jooil Kim⁴, Shanlan Li⁵, Helen Webster³, David Thomson³, Jens Mühle⁴, Ray F. Weiss⁴, Sunyoung Park^{5,6}, and Simon O'Doherty⁷

5

¹National Physical Laboratory, Teddington, Middlesex, UK

²School of GeoSciences, University of Edinburgh, Edinburgh, UK

³Met Office, Exeter, UK

⁴Scripps Institution of Oceanography, University of California, San Diego, La Jolla,
10 California 92037, USA

⁵Kyungpook Institute of Oceanography, Kyungpook National University, Daegu 41566,
Republic of Korea

⁶Department of Oceanography, Kyungpook National University, Daegu 41566, Republic of
Korea

15 ⁷School of Chemistry, University of Bristol, Bristol, UK.

*Corresponding author tim.arnold@ed.ac.uk

Decadal trends in the atmospheric abundances of carbon tetrafluoride (CF₄) and nitrogen
trifluoride (NF₃) have been well characterised and have provided a time series of global total
20 emissions. Information on locations of emissions contributing to the global total, however, is
currently poor. We use a unique set of measurements between 2008 and 2015 from the Gosan
station, Jeju Island, South Korea (part of the Advanced Global Atmospheric Gases
Experiment network), together with an atmospheric transport model to make spatially
disaggregated emission estimates of these gases in East Asia. Owing to the poor availability
25 of good prior information for this study our emissions estimates are largely influenced by the
atmospheric measurements. Notably, we are able to highlight emissions hotspots of NF₃ and
CF₄ in South Korea, owing to the measurement location. We calculate emissions of CF₄ to be
quite constant between years 2008 and 2015 for both China and South Korea with 2015
emissions calculated at 4.3 ± 2.7 Gg yr⁻¹ and 0.36 ± 0.11 Gg yr⁻¹, respectively. Emission

30 estimates of NF_3 from South Korea could be made with relatively small uncertainty at $0.6 \pm 0.07 \text{ Gg yr}^{-1}$ in 2015, which equates to $\sim 1.6\%$ of the country's CO_2 emissions. We also apply our method to calculate emissions of CHF_3 (HFC-23) between 2008 and 2012, for which our results find good agreement with other studies and which helps support our choice in methodology for CF_4 and NF_3 .

35 **1. Introduction**

The major greenhouse gases (GHGs) – carbon dioxide, methane and nitrous oxide – have natural and anthropogenic sources. The synthetic fluorinated species (chlorofluorocarbons, hydrochlorofluorocarbons, hydrofluorocarbons, and perfluorocarbons) are almost or entirely anthropogenic and are released from industrial and domestic appliances and applications. Of the synthetic species, tetrafluoromethane (CF_4) and nitrogen trifluoride (NF_3) are emitted nearly exclusively from point sources of specialized industries (Arnold et al., 2013; Mühle et al., 2010). Although these species currently make up only a small percentage of current emissions contributing to global radiative forcing, they have potential to form large portions of specific company, sector, state, province, or even country level GHG budgets.

45 CF_4 is the longest-lived GHG gas known with an estimated lifetime of 50,000 years, leading to a global warming potential on a 100-year time scale (GWP_{100}) of 6630 (Myhre et al., 2013). Significant increases in atmospheric concentrations are ascribed mainly to emissions from primary aluminum production during so-called “anode events” when the alumina feed to the reduction cell is restricted (International Aluminium Institute, 2016), and from the microchip-manufacturing component of the semiconductor industry (Illuzzi and Thewissen, 2010). Recently, evidence is emerging that, similar to primary aluminium production, rare earth element production may also release substantial amounts of CF_4 (Vogel et al., 2017; Zhang et al., 2017). Other emission sources for CF_4 include release during the production of SF_6 and HCFC-22, but emissions from these sources are estimated to be small compared to the emissions from the aluminium production and semiconductor manufacturing industries (EC-JRC/PBL, 2013; Mühle et al., 2010). There is also a very small natural emission source of CF_4 , sufficient to maintain the preindustrial atmospheric burden (Deeds et al., 2008).

According to the IPCC fifth assessment, NF_3 's global warming potential on a 100-year time scale (GWP_{100}) is $\sim 16,100$ (based on an atmospheric lifetime of 500 years) (Myhre et al., 2013), however, recent work suggests the GWP_{100} is higher at 19,700 owing to an increased estimate in the radiative efficiency (Totterdill et al., 2016). Use of NF_3 began in the 1960s in

specialty applications, e.g., as a rocket fuel oxidizer and as a fluorine donor for chemical lasers (Bronfin and Hazlett, 1966). Beginning in the late 1990s, NF_3 has been used by the semiconductor industry, and in the production of photovoltaic cells and flat-panel displays.

65 NF_3 can be broken down into reactive fluorine (F) radicals and ions, which are used to remove the remaining silicon-containing deposits in process chambers (Henderson and Woytek, 1994; Johnson et al., 2000). NF_3 was also chosen because of its promise as an environmentally friendly alternative, with conversion efficiencies to create reactive F far higher than other compounds such as C_2F_6 (Johnson et al., 2000; International SEMATECH

70 Manufacturing Initiative, 2005). Given its rapid recent rise in the global atmosphere and projected future market, it has been estimated that NF_3 could become the fastest growing contributor to radiative forcing of all the synthetic GHGs by 2050 (Rigby et al., 2014b).

CF_4 and NF_3 are not the only species with major point source emissions. Trifluoromethane (CHF_3 ; HFC-23) is principally made as a byproduct in the production of

75 chlorodifluoromethane (CHClF_2 , HCFC-22). Of the hydrofluorocarbons (HFCs), HFC-23 has the highest 100-year global warming potential (GWP_{100}) at 12,400 owing most significantly to a long atmospheric lifetime of 222 years (Myhre et al., 2013). Its regional and global emissions have been the subject of numerous previous studies (Fang et al., 2014; McCulloch and Lindley, 2007; Miller et al., 2010; Montzka et al., 2010; Fang et al., 2015; Stohl et al.,

80 2010; Li et al., 2011; Kim et al., 2010; Yao et al., 2012; Keller et al., 2012; Yokouchi et al., 2006; Simmonds et al., 2018). Thus, emissions of HFC-23 are already relatively well characterized from a bottom up and top-down perspective. In this work we will also calculate HFC-23 emissions, not to add to current knowledge, but to provide a level of confidence for our methodology.

85 Unlike for HFC-23, the spatial distribution of emissions responsible for CF_4 and NF_3 abundances is very poorly understood, which is hindering action for targeting mitigation. HFC-23 is emitted from well-known sources (namely HCFC-22 production sites) with well characterized estimates of emission magnitudes and hence it has been a target for successful mitigation (by thermal destruction) via the clean development mechanism (Miller et al.,

90 2010). However, emissions of CF_4 and NF_3 are very difficult to estimate from industry level information: Emissions from Al production are highly variable depending on the conditions of manufacturing, and emissions from the electronics industry depend on what is being manufactured, the company's recipes for production (such information is not publicly available) and whether abatement methods are used and how efficient these are under real

95 conditions. Both the Al production and semiconductor industries have launched voluntary
efforts to control their emissions of these substances, reporting success in meeting their goals
(International Aluminium Institute, 2016; Illuzzi and Thewissen, 2010; World Semiconductor
Council, 2017). Despite the industry's efforts to reduce emissions, top-down studies on the
emissions of CF₄ and NF₃ have shown the bottom-up inventories are likely to be highly
100 inaccurate. Most recently, Kim et al. (2014) showed that global bottom-up estimates for CF₄
are as much as 50% lower than top-down estimates, and Arnold et al. (2013) show that the
best estimates of global NF₃ emissions calculated from industry information and statistical
data total only ~35% of that estimated from atmospheric measurements.

Accurate emission estimates of NF₃ and CF₄ are difficult to make based on simple parameters
105 such as integrated country level uptake rates and leakage rates, which, for example, underpin
calculations of HFC emissions. Active or passive activities to reduce emissions vary between
countries, and between industries and companies within countries, and the impetus to
accurately understand emissions is lacking in regions that have not been required to report
emissions under the UNFCCC. This problem is compounded by the difficulty in making
110 measurements of these gases: CF₄ and NF₃ are the two most volatile GHGs after methane
(CH₄) with low atmospheric abundances, which makes routine measurements in the field at
the required precision particularly difficult. The Advanced Global Atmospheric Gases
Experiment (AGAGE) has been monitoring the global atmospheric trace gas budget for
decades (Prinn et al., 2018). Most recently, AGAGE's 'Medusa' pre-concentration GC-MS
115 (gas chromatography-mass spectrometry) system has been able to measure a full suite of the
long-lived halogenated GHGs (Arnold et al., 2012; Miller et al., 2008). The Medusa is the
only instrument demonstrated to measure NF₃ in ambient air samples, and the only field-
deployable instrument capable of measuring CF₄. The Medusa on Jeju Island, South Korea is
one of only twenty such instruments currently in operation globally and is uniquely sensitive
120 to the dominant emission sources of these compounds given its location in this highly
industrial part of the globe with large capacities of Al production, semiconductor
manufacturing, and rare earth element production industries. Its utility has already been
demonstrated in numerous previous studies to understand emissions of many GHGs from
Japan, South Korea, North Korea, eastern China, and surrounding countries (Fang et al.,
125 2015; Kim et al., 2010; Li et al., 2011).

For the first time we use the measurements of CF₄ (starting in 2008) and NF₃ (starting in
2013) in an inversion framework – coupling each measurement with an air history map

computed using a particle dispersion model. We demonstrate the use of these measurements to find emissions hotspots in this unique region with minimal use of prior information, and we show that East Asia is a major source of these species. Focussed mitigation efforts, based on these results, could have a significant impact on reducing GHG emissions from specific areas. The technology for abating emissions of these gases from such discrete sources exists and could be used (Chang and Chang, 2006; Purohit and Höglund-Isaksson, 2017; Illuzzi and Thewissen, 2010; Yang et al., 2009; Raoux, 2007; Wangxing et al., 2016).

135

2. Methods

2.1 Atmospheric measurements

The Gosan station (from here on termed GSN) is located on the south-western tip of Jeju Island in the Republic of Korea (126.16181° E, 33.29244° N). The station rests at the top of a 72 m cliff, about 100 km south of the Korean peninsula, 500 km northeast of Shanghai, China, and 250 km west of Kyushu, Japan, with an air inlet 17 m above ground level.

140

A Medusa GC-MS system was installed at GSN in 2007 and has been operated as part of the AGAGE network to take automated, high-precision measurements for a wide range of CFCs, HCFCs, HFCs, PFCs, Halons and other halocarbons; all significant synthetic GHG and/or stratospheric ozone depleting gases as well as many naturally occurring halogenated compounds (Miller et al., 2008; Arnold et al., 2012; Kim et al., 2010). Since November 2013, NF_3 has been measured within this suite of gases. Air reaches GSN from the most heavily developed areas of East Asia, making the measurements and their interpretation a unique source for ‘top-down’ emissions estimates in the region. Ambient air measurements are made every 130 minutes and are bracketed with a standard before and after the air sample to correct for instrumental drift in calibration. Further details on the methodology for the calibration of these gases are given elsewhere (Arnold et al., 2012; Mühle et al., 2010; Miller et al., 2010; Prinn et al., 2018).

145

150

2.2 Atmospheric model

Lagrangian particle dispersion models are well suited to determine emissions of trace gases on this spatial scale as they can be run backwards allowing for the source-receptor relationship to be efficiently calculated. We use the Numerical Atmospheric dispersion Modelling Environment (NAME III), henceforth called NAME, developed by the UK Met Office (Ryall and Maryon, 1998; Jones et al., 2007). Inert particles are advected backwards in

155

160 time by the transport model, NAME, which also associates a mass to each trajectory. Hence, NAME output is provided as the time integrated near-surface (0 - 40 m) air concentration (g s m^{-3}) in each grid cell – the surface influence resulting from a conceptual release at a specific rate (g s^{-1}) from the site. ‘Offline’ this surface influence is divided by the total mass emitted during the 1-hour release time and multiplied by the geographical area of each grid box to
165 form a new array with each component representative of how $1 \text{ g m}^{-2} \text{ s}^{-1}$ of continuous emissions from a grid square would result in a measured concentration at the model’s release point (the measurement site). Multiplication of each grid component by an emission rate then results in a contribution to the concentration.

The meteorological parameter inputs to NAME are from the Met Office’s operational global
170 NWP model, the Unified Model (UM) (Cullen, 1993). The UM had a horizontal resolution of $0.5625^\circ \times 0.375^\circ$ ($\sim 40 \text{ km}$) from December 2007 to April 2010; $0.3516^\circ \times 0.2344^\circ$ ($\sim 25 \text{ km}$) from April 2010 to July 2014; and $0.234375^\circ \times 0.15625^\circ$ ($\sim 17 \text{ km}$) from mid-July 2014 to mid-July 2017. The number of vertical levels in the UM has increased over this period, with NAME taking the lowest 31 levels in 2009 and the lowest 59 levels in 2015. The GHGs
175 considered in this study have lifetimes on the order of hundreds to tens of thousands of years (Myhre et al., 2013), and can be considered inert gases on the spatial and temporal scales of this study and therefore the NAME model schemes for representing chemistry, dry deposition, wet deposition and radioactive decay were not used. The boundary layer height (BLH) estimates are taken from the UM, however, a minimum BLH allowed within NAME
180 was set to 40 m to be consistent with the maximum emission height and the height of the output grid. The NAME model was run to estimate the 30-day history of the air on route to GSN. We calculated the time-integrated air concentration (dosage) at each grid box ($0.352^\circ \times 0.234^\circ$, and 0–40 m above ground level, irrespective of the underlying UM meteorology resolution) from a release of 1 g s^{-1} at GSN at 10 ± 10 metres above the model ground level
185 (magl).

The model is three-dimensional, and therefore it is not just surface to surface transport that is modelled: An air parcel can travel from the surface to a high altitude and then back to the surface but only those times when the air parcel is within the lowest 40 m above the ground will it be included in the model output aggregated sensitivity maps. The computational
190 domain covers 54.34° E to 168.028° W longitude (391 grid cells of dimension 0.352°) and 5.3° S to 74.26° N latitude (340 grid cells of dimension 0.234°) and extends to more than 19 km vertically. Despite the increase in the resolution of the UM over the time period covered,

the resolution of the NAME output was kept constant throughout. For each 1 h period, 5000 inert model particles were used to describe the dispersion of air. By dividing the dosage [g s m^{-3}] by the total mass emitted [$3600 \text{ s h}^{-1} \times 1 \text{ h} \times 1 \text{ g s}^{-1}$] and multiplying by the geographical area of each grid box [m^2], the model output was converted into a dilution matrix H [s m^{-1}]. In figure 1 we show an aggregated dilution matrix for the 2013 inversion period, demonstrating the areas of most significant influence on the GSN measurements. Each element of the matrix H dilutes a continuous emission of $1 \text{ g m}^{-2} \text{ s}^{-1}$ from a given grid box over the previous 30 d to simulate an average concentration [g m^{-3}] at the receptor (measurement point) during a 1 h period.

2.3 Inversion framework

For most long-lived trace gases (with lifetimes of years or longer), the assumption that atmospheric mole fractions respond linearly to changes in emissions holds well. By using this linearity, we can relate a vector of observations (y) to a state vector (x) made up of emissions and other non-prescribed model conditions (see section 2.6), via a sensitivity matrix (H) (Tarantola, 2005):

$$y = Hx + \textit{residual}$$

A Bayesian framework is typically used in trace gas inversions and incorporates a priori information, which gives rise to the following cost function:

$$C = (Hx - y)^T R^{-1} (Hx - y) + (x - x_p)^T B^{-1} (x - x_p) \quad (1)$$

Where, C is the cost function score (the aim is to minimise this score); H is made up mainly of the model derived dilution matrices (Section 2.2) but also the sensitivity of changes in domain border conditions on measured mixing ratios; x is a vector of emissions and domain border conditions; y is a vector of observations; R is a matrix of combined model and observation uncertainties; x_p is a vector of prior estimates of emissions and domain border conditions; and B is an error matrix associated with x_p . The cost function is minimised using a “NNLS”, non-negative least squares fit (Lawson and Hanson, 1974), as previously used for volcanic ash (Thomson et al., 2017; Webster et al., 2017). The NNLS algorithm finds the least squares fit under the constraint that the emissions are non-negative. This is an "active set" method which efficiently iterates over choices for the set of emissions for which the non-negative constraint is active, i.e. the set of emissions which are set to zero.

The first term in equation 1 describes the mismatch (fit) between the modelled time-series and the observed time-series at each observation station. The observed concentrations (y) are comprised of two distinct components; (a) the Northern Hemisphere (NH) background concentration, referred to as the baseline, that changes only slowly over time, and (b) rapidly varying perturbations above the baseline. These observed deviations above background (baseline) are assumed to be caused by emissions on a regional scale that have yet to be fully mixed on the hemisphere scale. The magnitude of these deviations from baseline and, crucially, how they change as the air arriving at the stations travels over different areas, is the key to understanding where the emissions have occurred. The inversion system considers all of these changes in the magnitude of the deviations from baseline as it searches for the best match between the observations and the modelled time-series. The second term describes the mismatch (fit) between the estimated emissions and domain border conditions (x) and prior estimated emissions and domain border conditions (x_p) considering the associated uncertainties (B).

The aim of the inversion method is to estimate the spatial distribution of emissions across a defined geographical area. The emissions are assumed to be constant in time over the inversion time period (in this case one calendar year as is typically reported in inventories). Assuming the emissions are invariant over long periods of time is a simplification, but is necessary given the limited number of observations available. In order to compare the measurements and the model time-series, the latter are converted from air concentration [g m^{-3}] to the measured mole fraction (e.g. parts per trillion [ppt]) using the modelled temperature and pressure at the observation point.

2.4 Prior emissions information

Global emissions estimates of CF_4 and NF_3 using atmospheric measurements have demonstrated that ‘bottom-up’ accounting methods for one or more sectors, or one or more regions, are highly inaccurate (Arnold et al., 2013; Mühle et al., 2010). This study makes no effort to improve such inventory methods but instead focuses on minimising the reliance of prior information on our Bayesian-based posterior emissions estimates. Our prior information data sets come from the EDGAR (Emissions Database for Atmospheric Research) v4.2 emission grid maps (EC-JRC/PBL, 2013). This data set only covers the years 2000 to 2010 and therefore we apply the prior for 2010 for each year between 2011 and 2015. The $0.1 \times 0.1^\circ$ EDGAR emission maps were first re-gridded based on the lower resolution of our inversion grid ($0.3516^\circ \times 0.2344^\circ$). In order to remove the influence of the within-country

prior spatial emissions distribution, each country's emissions were then averaged across their entire landmass (see Figure S1). We applied 5 different levels of uncertainty to each inversion grid cell (a,b) in 5 separate inversion experiments, each a multiple of the emissions magnitude ($x_{a,b}$) in each grid cell: $1 \times x_{a,b}$ (i.e. 100% uncertainty), $10 \times x_{a,b}$, $100 \times x_{a,b}$, $1000 \times x_{a,b}$, and $10,000 \times x_{a,b}$. We were then able to test the sensitivity of the prior emissions uncertainty and provide evidence for the low influence of prior information on the emissions estimates in the posterior.

2.5 Model-measurement and prior uncertainties

In addition to inaccurate prior information, another significant source of uncertainty in estimating emissions is from the model; from both the input meteorology and the atmospheric transport model itself. The uncertainty matrix, R , is a critical part of equation 1 that allows us to adjust uncertainties assigned to each measurement depending on how well we think the model is performing at that time: It describes, per hour time period, a combined uncertainty of the model and the observation at each time. The method of assigning measurement-model uncertainties is under development and here we describe one method that has been applied to the modelling of GSN measurements. All elements of the modelled meteorology (wind speed and direction, boundary layer height, temperature, pressure, etc.) are important in understanding the dilution and uncertainty in modelling from source to receptor, however, quantifying the impact of each element that each model particle experiences in order to fully quantify the model uncertainty at each measurement time is beyond what is available from numerical weather prediction models. So in order to attempt to quantify a model/observation uncertainty we took a pragmatic approach and used modelled boundary layer height at the receptor as a proxy.

Emissions are primarily diluted by transport and mixing within the planetary boundary layer (PBL), and hence, modelling of the PBL height (BLH) is crucial for accurate modelling of the mixing ratios. Changes in boundary layer height at or surrounding the measurement location can cause significant changes to the measured mixing ratio. A low boundary layer (causing a larger model uncertainty) has two implications for measurements at the Gosan site: 1) A greater possibility of air from above the boundary layer being sampled in reality but not in the model. Subtle changes in the boundary layer height at the exact measurement location are not well modelled and the difference between sampling above or below the boundary layer can have a significant influence on the amount of pollutant assigned to a back trajectory. 2) Greater influence of emissions from sources very near GSN. A lower boundary layer means that a

290 lower rate of dilution of local emissions will occur, in turn increasing the signal of the local
pollutant above the baseline. A relatively small change in a low boundary layer will have a
significant influence on this dilution compared to the same change on a high boundary layer.
Thus, any error in the boundary layer height at low levels can significantly amplify the
uncertainty in the pollutant dilution. This is coupled with the fact that the modelled boundary
295 layer has significant uncertainty especially when low.

To assign a model uncertainty to each hourly window of measurements we use model
information of BLH:

$$\sigma_{model} = \sigma_{baseline} \times f_{BLH} \quad (3)$$

where, $\sigma_{baseline}$ is the variability associated with the baseline calculation (see Section 2.6),
300 and f_{BLH} is a multiplying factor (greater than or less than unity) that increases or decreases
the relative uncertainty assigned to each model time period. f_{BLH} is based on modelled
boundary layer height magnitude and variability over a three-hour period and is calculated
with the following:

$$f_{BLH} = \frac{Max_{BLH-inlet}}{Min_{BLH-inlet}} \times \frac{Threshold}{Min_{BLH}}$$

305 where, $Max_{BLH-inlet}$ is the largest of either 100 m or the maximum distance, calculated
hourly, between the inlet and the modelled BLH within a period of three hours around the
measurement time; $Min_{BLH-inlet}$ is the smallest of the distances calculated between the inlet
and the BLH over the same three-hour period; $Threshold$ is an arbitrary value set at 500 m;
and Min_{BLH} is the lowest boundary layer height recorded over the three-hour period. Thus,
310 the relative assigned uncertainty considers the proximity of the varying boundary layer to the
inlet height and a recognition that observations taken when the boundary layer is varying at
higher altitudes (>500 m a.g.l.) is likely to have less impact and therefore have lower
uncertainty compared to those taken when the BLH is varying at lower altitudes (< 500
magl).

315 Supporting Figures S2-S6 show annual time series of observations and the corresponding
measurement-model uncertainties, as well as statistics for the mismatch between observations
and modelled time series.

2.6 Baseline calculation and domain border conditions

For each measurement at GSN it is important to accurately understand the portion of the total
320 mixing ratio arriving from outside the inversion domain and the portion from emission
sources within the domain, otherwise emissions from specific areas could be over or under
estimated. GSN is uniquely situated; receiving air masses from all directions over the course
of the year, which can have distinct compositions of trace gases, driven mainly by the
different emission rates between the two hemispheres and slow inter-hemispheric mixing.

325 In addition to the time integrated air concentration produced by NAME (Section 2.2), the 3D
coordinate where each particle left the computational domain was also recorded. This
information was then post-processed to produce the percentage contributions from 11
different borders of the 3D domain (Figure 2). From 0 to 6 km in height eight horizontal
boundaries (WSW, WNW, NNW, NNE, ENE, ESE, SSE, SSW) were considered and
330 between 6 to 9 km the horizontal boundaries were only split between north and south. The
eleventh border was considered when particles left in any direction above 9 km. Thus, the
influence of air arriving to GSN from outside the domain was simplified as a combination of
air masses arriving from 11 discrete directions.

We use measurements from the Mace Head observatory (from here termed MHD) on the
335 west coast of Ireland (53.33° N, 9.90° W) – a key AGAGE (Advanced Global Atmospheric
Gases Experiment) site providing long term in-situ atmospheric measurements – to act as a
starting point for an estimate of the composition of air from the NH mid-latitudes entering the
East Asia domain. MHD was one of the first locations to measure CF_4 (starting 2004) and
 NF_3 (starting 2012) and other measurements from the site are routinely used in atmospheric
340 studies to calculate decadal trends in the NH atmospheric abundances. In summary, a
quadratic fit was made only to MHD observations that were representative of the NH
baseline. i.e. when well mixed air was arriving predominately from the WNW-NNW (North
Atlantic) direction as calculated using NAME (details of filtering and fitting are given in the
Supporting Text).

345 The composition of air arriving from any of the 11 directions is calculated using
corresponding multiplying factors applied to the MHD baseline, which were included as part
of the state vector (x), i.e. these factors are constant for a given inversion year. The prior
baseline was therefore perturbed as part of the inversion based on the relative contribution of
air arriving from different borders of the 3D domain and the multiplying factors that are
350 included within the cost function (Equation 2). Figure 3 shows an annual time series of

observations for CF₄ and the difference between the prior baseline (the quadratic fit from MHD) and the posterior baseline.

2.7 Domains and inversion grids

355 The domain used in the inversion is smaller than the computational NAME transport model domain. The horizontal inversion domain covers 88.132° E to 145.860° E longitude (164 fine grid cells of 0.352°) and 15.994° N to 57.646° N latitude (178 fine grid cells of 0.234°). As GSN is surrounded by highly industrial areas the site is insensitive to small emissions or highly diluted emissions from further away. NAME is run on a larger domain to ensure that on the occasion when air circulates out of the inversion domain and then back, its full 30-day history in the inversion domain is included.

360 An initial computational inversion grid (from here termed the ‘coarse grid’) was created based on a) aggregated information from the NAME footprints over the period of the inversion (in this case one year), aggregating fewer grid cells in areas that are ‘seen’ the most by GSN, and b) on the prior emissions flux i.e. areas known to have low emissions (i.e. the ocean) had higher aggregation. Course grid cells could not be aggregated over more than a single country/region and a total of ≈100 coarse grid cells (n) were created. After the initial inversion the posterior emissions density [g yr⁻¹ m⁻²] and the ability of the posterior emissions to impact the measurements at GSN (using information from the NAME output) was used to choose a coarse grid cell to divide in two by area. A new inversion was run using identical 370 inputs except for the number of grid cells (now n+1). This sequence was repeated 50 times creating ≈150 coarse grid cells within the inversion domain for the final inversion. The results from the inversions with the maximum disaggregation are presented in this paper.

3. Results and discussion

3.1 Country total emissions estimates

375 Table 1 provides a summary of our estimates of emissions from the five major emitting countries/regions within the East Asia domain. These posterior emission estimates use a prior emissions uncertainty in each fine grid cell of 100x the emissions magnitude (see Section 2.4).

HFC-23

380 Fang et al. (2015) conducted a very thorough ‘bottom-up’ study within their work on HFC-23; constraining an inversion model using both prior information and atmospheric

measurements. They used an inverse method based on FLEXPART using measurements from three sites in East Asia – GSN, Hateruma (a Japanese island ~200 km east of Taiwan), and Cape Ochi-ishi (northern Japan), calculating an HFC-23 emissions rise in China from 6.4 ± 0.7 Gg yr⁻¹ in 2007 (6.2 ± 0.6 Gg yr⁻¹ in 2008) to 8.8 ± 0.8 Gg yr⁻¹ in 2012. An earlier study by Stohl et al. (2010) also report HFC-23 emissions of 6.2 ± 0.8 Gg yr⁻¹ in 2008. Both Fang et al. (2015) and Stohl et al. (2010) report emissions from other countries below 0.25 Gg yr⁻¹ for all years. Our estimates use a completely independent inverse method and only data from GSN, yet the results are very close to those from Fang et al. (2015) (Figure 4): 6.8 ± 4.3 Gg yr⁻¹ in 2008 (a difference of 10%) and 10.7 ± 4.6 Gg yr⁻¹ in 2012 (a difference of 22%), and to Stohl et al. (2010). The posterior uncertainties in these two different studies mainly reflect the difference in the prior uncertainty assumed for the prior information: We assume a very high level of uncertainty on our prior emissions and therefore our posterior uncertainties are significantly higher. However, these inversion result estimates are lower than estimates based on inter-species correlation analysis by Li et al. (2011) who calculated emissions of HFC-23 from China in 2008 in the range of 7.2-13 Gg yr⁻¹. And using a CO tracer-ratio method, Yao et al. (2012) estimated particularly low emissions of 2.1 ± 4.6 Gg yr⁻¹ for 2011-2012. The estimates derived from atmospheric inversions do not rely on any correlations with other species or known emissions for certain species, and given two separate inversion studies have produced very similar results we suggest these provide a more reliable ‘top-down’ emissions estimate of HFC-23. As well as providing an independent validation of the previous work on HFC-23 by Fang et al. (2015) and Stohl et al. (2010), the alignment of our HFC-23 emissions estimates with those previous studies provides confidence in our inversion methodology for the CF₄ and NF₃ emissions estimates.

405 *CF₄*

Our understanding of emissions of CF₄ and NF₃ is very poor, which is highlighted in global studies based on atmospheric measurements that show bottom-up estimates of emissions are significantly underestimated (Möhle et al., 2010; Arnold et al., 2013). With such a poor prior understanding of emissions we assess the effect of prior uncertainty on the posterior emissions (Figure 4). With assignment of uncertainty on the prior of each fine grid cell at ten times the prior emissions value, the posterior is still significantly constrained by the prior for both China and South Korea. Posterior estimates when larger uncertainties are applied to the prior (100x to 10000x) are very consistent, indicating that when greater than 100x uncertainty is applied, emissions estimates are most significantly constrained by the atmospheric

415 measurements. For China for 7 of the 8 years studied our posterior estimates are greater than
twice the prior estimates taken from EDGAR v4.2. The latest global estimates are from
Rigby et al. (2014) and they estimated global CF₄ emissions of 10.4±0.6 Gg/year in 2008
with a steady but small increase to 11.1 ± 0.4 Gg/year in 2013 (with the exception of a dip in
2009 to 9.3±0.5 Gg/year). We highlight that our Chinese emission estimates remain within a
420 narrow range for 5 of the 8 years studied at between 4.0 and 4.7 Gg/year (with typical
uncertainties <2.7 Gg/year), and for 7 of the 8 years studied between 2.82 and 5.35 Gg/year.
However, the estimate for 2012 appears to be anomalous at 8.25±2.59 Gg/year. In relation to
the global top-down estimates from 2008 to 2012, our Chinese estimates represent between
37 to 45 % of global emissions between 2008 and 2011 with a jump to 74 % in 2012. This
425 significant increase in 2012 is not reconcilable with atmospheric measurements on the global
scale and is very likely a spurious result of the inversion. The most probable explanation for
such a result is the incorrect assignment of emissions on the inversion grid. Incorrect
assignment of emissions can occur between countries, particularly where air parcels
frequently pass over more than one country, therefore reducing the ability of the inversion to
430 confidently place emissions. However, there is not an obvious drop in emissions for another
country in 2012 that would offset the large increase in the Chinese emissions estimate.
Within a country, incorrect assignment of emissions from an area closer to the receptor to an
area further from the receptor will increase the calculated total emissions owing to increased
dilution in going from a near to a far source. Our inversion is susceptible to this effect as we
435 only have one site for assimilation of measurements; two measurement sites, spaced apart
and straddling the area of interest, would provide significantly more information to constrain
the spatial emissions distribution.

Our estimates are significantly higher than emission estimation methods using interspecies
440 correlation: Kim et al. (2010) estimated CF₄ emissions in the range of only 1.7-3.1 Gg yr⁻¹ in
2008 and Li et al. (2011) only 1.4-2.9 Gg yr⁻¹ over the same period. The interspecies
correlation approach inherently requires that the sources of the different gases that are
compared are coincident in time and space. Kim et al. (2010) and Li et al. (2011) used
HCFC-22 as the tracer compound for China with a calculated emissions field from an inverse
445 model and most emissions of this gas originate from fugitive release from air conditioners
and refrigerators. However, CF₄ is emitted mostly from point sources in the semiconductor

and aluminium production industries with different spatial emissions distribution within countries, and likely different temporal characteristics compared to HCFC-22.

Emissions estimates from South Korea and Japan are one order of magnitude lower than for
450 China. For 2008 Li et al. (2011) estimate emissions of CF₄ from combined South and North
Korea of 0.19-0.26 Gg yr⁻¹ and from Japan of 0.2-0.3 Gg yr⁻¹, which are on the low end of the
uncertainty range of our estimates for that year (Table 1). As one of the largest, if not the
largest, country for semiconductor wafer production, Taiwan is also an emitter of CF₄.
However, measurements at GSN provide only poor sensitivity to detection of emissions from
455 Taiwan and our results can only suggest that emissions are likely <0.5 Gg yr⁻¹. North Korea
emissions were small and no annual estimate was above 0.1 Gg yr⁻¹.

NF₃

Our understanding of NF₃ emissions from inventory and industry data is even poorer than for
CF₄. On a global scale the emission estimates from industry are underestimated (Arnold et
460 al., 2013). This study suggests that at least some emissions of NF₃ stem from China, however
gaining meaningful quantitative estimates has been difficult due to large uncertainties (Figure
4). Contrastingly, the posterior estimates of emissions from South Korea have relatively
small uncertainties. Emissions from China travel a greater distance to the measurement site
compared to emissions from South Korea. Thus, the magnitude of NF₃ pollution events from
465 China (especially from provinces furthest west), in terms of the mixing ratio detected at GSN,
are smaller than for pollution arriving from neighbouring South Korea. Also, the poorer
measurement precision for NF₃ compared to CF₄ leads to a larger uncertainty on the baseline,
which in turn affects the certainty on the pollution episode, especially for more dilute signals.
Emissions estimates for Japan are difficult to make without improved prior information and
470 more atmospheric measurements in other locations. We argue that other large changes in our
emissions estimates from 2014 to 2015 could be real. For example, Japan's National
Inventory Report for NF₃ shows a reduction in emissions of 63% between 2013 and 2015
(Ministry of the Environment Japan et al., 2018), which is within the uncertainty of the
relative rate of decrease we observe.

475 As for CF₄, emission estimates of NF₃ from Taiwan and North Korea are highly uncertain.
However, our results do indicate that emissions of NF₃ from Taiwan might be lower than
from South Korea despite very similar sized semiconductor production industries. Focussing
on the more meaningful estimates from South Korea, emissions of NF₃ in 2015 are estimated

to be $0.60 \pm 0.07 \text{ Gg yr}^{-1}$ which equates to $9660 \pm 1127 \text{ Gg yr}^{-1}$ CO₂-equivalent emissions
480 (based on a GWP₁₀₀ of 16,100). This is ~1.6% of the country's CO₂ emissions (Olivier et al.,
2017), thus making a significant impact on their total GHG budget. Further, given that the
sources of NF₃ are relatively few, these emissions can be assigned to a small number of
industries, potentially making NF₃ an easy target for focussed mitigation policy. Rigby et al.
(2014a) updated the global emission estimates from Arnold et al. (2013), calculated an annual
485 emissions estimate of 1.61 Gg yr^{-1} for 2012, with an average annual growth rate over the
previous 5 years of 0.18 Gg yr^{-1} . Linearly extrapolating this growth to 2014 and 2015 leads to
projected global emissions of 1.97 and 2.15 Gg yr^{-1} for 2014 and 2015, respectively. Thus,
South Korean emissions as a percentage of these global totals equate to ~20% and ~28% for
2014 and 2015, respectively, which is around the proportion of semiconductor wafer
490 fabrication capacity in South Korea relative to global totals (~20%) (SEMI, 2017).

3.2 Spatial emission maps

We use 'emissions minus uncertainty' maps (e.g. Figure 5B) is to provide information on
where we are most certain of large emissions i.e. where emission hotspots are located and if
495 they are significant: Less negative values indicate more certainty, with positive values
indicating that the uncertainty is less than the best estimate and negative values indicating
that the uncertainty is bigger than the estimate. A more common way to illustrate grid-level
uncertainty is in an 'uncertainty reduction' map. This works well when starting from a
relatively well-constrained, spatially resolved prior to illustrate the additional constraint the
500 atmospheric observations add. In this study, however, we are starting from very poor prior
information and we generate a posterior emission map that is very distinct from the prior,
informed largely by the measurements. Thus, an uncertainty reduction map provides little
useful information.

Figure 5 shows the effect of re-gridding over the course of 50 separate CF₄ inversions (for
505 2015), from zero re-gridding steps (i.e. using a coarse grid space determined using
information from NAME and the prior emissions), through to 25, and then 50 steps. The
inversion was not allowed to decrease the minimum posterior grid size beyond four fine grid
squares (i.e. four times the $0.3516^\circ \times 0.2344^\circ$ grid square). This method highlights the areas
that have the highest emissions density; the splitting of these grid cells improves the
510 correlation between observations and posterior model output. However, these emission maps

must be studied alongside the corresponding uncertainty maps. The inversion could continue to split towards a fine grid resolution limit even though there may not be enough information in the data to accurately constrain emissions from each coarse grid cell (leading to spurious emission patterns) and the process would be computationally very expensive. The largest emissions of CF₄ arise from China and Figure 5 suggests the largest emissions come from an area between 35° N and 38° N. The uncertainty on these emissions from the specific final coarse grid squares is large (Figure 5F) and therefore care needs to be taken not to over interpret emission hotspots. Although the grid is being split it is not realistic for the model to correctly interpret the spatial distribution of emissions at this distance from GSN, and this is demonstrated in Figure 5F where the relative error on emissions in this corner of the domain is large. Without better prior information it is not possible to distinguish between real year-to-year emission pattern changes and inaccurate emission patterns (Figure 6 and S7). Over the period of study emissions of CF₄ generally appear to arise from north of 30° and in 2008 and 2013 emissions appear around 25° N. However, GSN does not have good sensitivity to emissions from this area and it is possible that these emissions could be incorrectly assigned from Taiwan. Although emissions from South Korea are significantly lower than for China, the proximity to GSN causes the grid cells to be split and emissions to be assigned at higher spatial resolution, and generally (except for 2008) in the north-west quadrant of the country. Splitting of grid cells in South Korea decreased the relative error on the emissions from particular grid squares, providing confidence that the placement of emissions is accurate. Further, for sequential years 2013, 2014 and 2015 two specific grid cells in that north-west quadrant are highlighted with comparatively low uncertainties (Figure S7). How well these consistent year-to-year emission patterns in South Korea correlate with the actual location of emissions needs to be the subject of further study (e.g. improved bottom-up inventory compilation efforts). Emissions from Japan are too uncertain to explore the spatial emissions pattern.

For NF₃, emissions from China and Japan are too low and uncertain to interpret at finer spatial resolution. However, as with CF₄, it is interesting to study the relatively more certain spatially disaggregated emissions from South Korea (Figure 7). In common with CF₄, NF₃ emissions from the south-west area are minimal, however in contrast to CF₄, emissions occur on the eastern side of South Korea and on the south east coast. Emissions from the south east coast coincide with the known location of a production plant for NF₃ located in the area of Ulsan (Gas World, 2011). If this plant is sufficiently separated in space from the end-users of

NF₃ then this result would indicate that production of NF₃, not just use, could be a significant source in South Korea.

The study of Fang et al. (2015) highlights three major hotspots for HFC-23 emissions in China based on HCFC-22 production facility locations. Our posterior maps (Figure 8) correctly show the bulk of emissions in far eastern China, in line with the results of Fang et al. (2015). However, given the inconsistency of emissions maps between years we are unable to provide any more information without a better spatially disaggregated prior emissions map.

Conclusions

We largely remove the influence of ‘bottom-up’ information and present the first Bayesian inversion estimates of CF₄ and NF₃ from the East Asia region using measurements from a single atmospheric monitoring site, GSN station located on the island of Jeju (South Korea). The largest CF₄ emissions are from China, estimated at 4-6 Gg yr⁻¹ for six out of the eight years studied, which is significantly larger than previous estimates. Despite significantly smaller emissions from South Korea, the spatial disaggregation of CF₄ emissions were consistent between independent inversions based on annual measurement data sets, indicating the north west of South Korea is a hotspot for significant CF₄ release, presumably from the semiconductor industry. Emissions of NF₃ from South Korea were quantifiable with significant certainty, and represent large emissions on a CO₂-equivalent basis (~1.6% of South Korea’s CO₂ emissions in 2015). HFC-23 emissions were also calculated using the same inversion methodology with high uncertainty on prior information. We found good agreement with other studies in terms of aggregated country totals and spatial emissions patterns, providing confidence that our methodology is suitable and conclusions justified for estimates of CF₄ and NF₃.

Our results highlight an inadequacy in both the bottom-up reported estimates for CF₄ and NF₃ and the limitations of the current measurement infrastructure for ‘top-down’ estimates for these specific gases. Adequate bottom-up estimates have been lacking, owing to the absence of reporting requirements for these gases from China and South Korea, and top-down estimates have been hampered by poor measurement coverage owing to the technical complexities required to measure these volatile, low abundance gases at high precision. Improvements in both bottom-up information and measurement coverage, alongside

refinements in transport modelling and developments in inversion methodologies, will lead to improved optimal emissions estimates of these gases in future studies.

580 **Acknowledgements**

Observations at GSN were supported by the Basic Science Research Program through the National Research Foundation of Korea (NRF) funded by the Ministry of Science, ICT & Future Planning (2014R1A1A3051944). The UK's Department for Business, Energy & Industrial Strategy (BEIS) funded the MHD measurements and the development of InTEM.

585

References

Arnold, T., Mühle, J., Salameh, P. K., Harth, C. M., Ivy, D. J., and Weiss, R. F.: Automated measurement of nitrogen trifluoride in ambient air, *Anal. Chem.*, 84, 4798–4804, 10.1021/ac300373e, 2012.

590 Arnold, T., Harth, C., Mühle, J., Manning, A. J., Salameh, P., Kim, J., Ivy, D. J., Steele, L. P., Petrenko, V. V., Severinghaus, J. P., Baggenstos, D., and Weiss, R. F.: Nitrogen trifluoride global emissions estimated from updated atmospheric measurements, *Proceedings of the National Academy of Sciences*, 110, 2019–2034, 2013.

595 Bronfin, B. R., and Hazlett, R. N.: Synthesis of nitrogen fluorides in a plasma jet, *Industrial & Engineering Chemistry Fundamentals*, 5, 472-478, 10.1021/i160020a007, 1966.

Chang, M. B., and Chang, J.-S.: Abatement of PFCs from Semiconductor Manufacturing Processes by Nonthermal Plasma Technologies: A Critical Review, *Industrial & Engineering Chemistry Research*, 45, 4101-4109, 10.1021/ie051227b, 2006.

600 Cullen, M. J. P.: The unified forecast/climate model, *Meteorological Magazine*, 122, 81-94, 1993.

Deeds, D. A., Vollmer, M. K., Kulongoski, J. T., Miller, B. R., Mühle, J., Harth, C. M., Izbicki, J. A., Hilton, D. R., and Weiss, R. F.: Evidence for crustal degassing of CF₄ and SF₆ in Mojave Desert groundwaters, *Geochimica et Cosmochimica Acta*, 72, 999-1013, 10.1016/j.gca.2007.11.027, 2008.

605 EC-JRC/PBL: Emission Database for Global Atmospheric Research (EDGAR), release version 4.2. In: <http://edgar.jrc.ec.europa.eu/>, Source: European Commission, Joint Research Centre (JRC)/Netherlands Environmental Assessment Agency (PBL), 2013.

610 Fang, X., Miller, B. R., Su, S., Wu, J., Zhang, J., and Hu, J.: Historical Emissions of HFC-23 (CHF₃) in China and Projections upon Policy Options by 2050, *Environ. Sci. Technol.*, 48, 4056-4062, 10.1021/es404995f, 2014.

Fang, X., Stohl, A., Yokouchi, Y., Kim, J., Li, S., Saito, T., Park, S., and Hu, J.: Multiannual Top-Down Estimate of HFC-23 Emissions in East Asia, *Environ. Sci. Technol.*, 49, 4345-4353, 10.1021/es505669j, 2015.

Gas World: Air Products doubles NF₃ facility at Ulsan, Korea. 2011.

- 615 Henderson, P. B., and Woytek, A. J.: Nitrogen–nitrogen trifluoride, in: Kirk–Othmer Encyclopedia of Chemical Technology, 4th ed., edited by: Kroschwitz, J. I., and Howe-Grant, M., John Wiley & Sons, New York, 1994.
- Illuzzi, F., and Thewissen, H.: Perfluorocompounds emission reduction by the semiconductor industry, *Journal of Integrative Environmental Sciences*, 7, 201-210, 10.1080/19438151003621417, 2010.
- 620 International Aluminium Institute: The International Aluminium Institute Report on the Aluminium Industry’s Global Perfluorocarbon Gas Emissions Reduction Programme – Results of the 2015 Anode Effect Survey, International Aluminum Institute, London, 1–56, 2016.
- 625 International SEMATECH Manufacturing Initiative: Reduction of Perfluorocompound (PFC) Emissions: 2005 State of the Technology Report, International SEMATECH Manufacturing Initiative, 2005.
- Johnson, A. D., Entley, W. R., and Maroulis, P. J.: Reducing PFC gas emissions from CVD chamber cleaning, *Solid State Technology*, 43, 103-114, 2000.
- 630 Jones, A., Thomson, D., Hort, M., and Devenish, B.: The UK Met Office's next-generation atmospheric dispersion model, NAME III, *Air Pollution Modeling and Its Applications Xvii*, edited by: Borrego, C., and Norman, A. L., 580-589 pp., 2007.
- Keller, C. A., Hill, M., Vollmer, M. K., Henne, S., Brunner, D., Reimann, S., O'Doherty, S., Arduini, J., Maione, M., Ferenczi, Z., Haszpra, L., Manning, A. J., and Peter, T.: European Emissions of Halogenated Greenhouse Gases Inferred from Atmospheric Measurements, *Environ. Sci. Technol.*, 46, 217-225, 10.1021/es202453j, 2012.
- 635 Kim, J., Li, S., Kim, K. R., Stohl, A., Mühle, J., Kim, S. K., Park, M. K., Kang, D. J., Lee, G., Harth, C. M., Salameh, P. K., and Weiss, R. F.: Regional atmospheric emissions determined from measurements at Jeju Island, Korea: Halogenated compounds from China, *Geophys. Res. Lett.*, 37, L12801 10.1029/2010gl043263, 2010.
- 640 Kim, J., Fraser, P. J., Li, S., Muhle, J., Ganesan, A. L., Krummel, P. B., Steele, L. P., Park, S., Kim, S. K., Park, M. K., Arnold, T., Harth, C. M., Salameh, P. K., Prinn, R. G., Weiss, R. F., and Kim, K. R.: Quantifying aluminum and semiconductor industry perfluorocarbon emissions from atmospheric measurements, *Geophys. Res. Lett.*, 41, 4787-4794, 10.1002/2014gl059783, 2014.
- 645 Lawson, C. L., and Hanson, R. J.: *Solving Least Squares Problems*, Classics in Applied Mathematics, 1974.
- Li, S., Kim, J., Kim, K.-R., Muehle, J., Kim, S.-K., Park, M.-K., Stohl, A., Kang, D.-J., Arnold, T., Harth, C. M., Salameh, P. K., and Weiss, R. F.: Emissions of Halogenated Compounds in East Asia Determined from Measurements at Jeju Island, Korea, *Environ. Sci. Technol.*, 45, 5668-5675, 10.1021/es104124k, 2011.
- McCulloch, A., and Lindley, A. A.: Global emissions of HFC-23 estimated to year 2015, *Atmos. Environ.*, 41, 1560-1566, 10.1016/j.atmosenv.2006.02.021, 2007.

- 655 Miller, B. R., Weiss, R. F., Salameh, P. K., Tanhua, T., Grealley, B. R., Mühle, J., and Simmonds, P. G.: Medusa: A sample preconcentration and GC/MS detector system for in situ measurements of atmospheric trace halocarbons, hydrocarbons, and sulfur compounds, *Anal. Chem.*, 80, 1536–1545, 10.1021/ac702084k, 2008.
- 660 Miller, B. R., Rigby, M., Kuijpers, L. J. M., Krummel, P. B., Steele, L. P., Leist, M., Fraser, P. J., McCulloch, A., Harth, C., Salameh, P., Mühle, J., Weiss, R. F., Prinn, R. G., Wang, R. H. J., O'Doherty, S., Grealley, B. R., and Simmonds, P. G.: HFC-23 (CHF₃) emission trend response to HCFC-22 (CHClF₂) production and recent HFC-23 emission abatement measures, *Atmos. Chem. Phys.*, 10, 7875–7890, 10.5194/acp-10-7875-2010, 2010.
- 665 Ministry of the Environment Japan, Greenhouse Gas Inventory Office of Japan, Center for Global Environmental Research, and National Institute for Environmental Studies, J.: National Greenhouse Gas Inventory Report of JAPAN, 2018.
- Montzka, S. A., Kuijpers, L., Battle, M. O., Aydin, M., Verhulst, K. R., Saltzman, E. S., and Fahey, D. W.: Recent increases in global HFC-23 emissions, *Geophys. Res. Lett.*, 37, 10.1029/2009gl041195, 2010.
- 670 Mühle, J., Ganesan, A. L., Miller, B. R., Salameh, P. K., Harth, C. M., Grealley, B. R., Rigby, M., Porter, L. W., Steele, L. P., Trudinger, C. M., Krummel, P. B., O'Doherty, S., Fraser, P. J., Simmonds, P. G., Prinn, R. G., and Weiss, R. F.: Perfluorocarbons in the global atmosphere: tetrafluoromethane, hexafluoroethane, and octafluoropropane, *Atmos. Chem. Phys.*, 10, 5145–5164, 10.5194/acp-10-5145-2010, 2010.
- 675 Myhre, G., Shindell, D., Bréon, F.-M., Collins, W., Fuglestedt, J., Huang, J., Koch, D., Lamarque, J.-F., Lee, D., Mendoza, B., Nakajima, T., Robock, A., Stephens, G., Takemura, T., and Zhang, H.: Anthropogenic and Natural Radiative Forcing, in: *Climate Change 2013: The Physical Science Basis. Contribution of Working Group I to the Fifth Assessment Report of the Intergovernmental Panel on Climate Change*, edited by: Stocker, T. F., Qin, D., Plattner, G.-K., Tignor, M., Allen, S. K., Boschung, J., Nauels, A., Xia, Y., Bex, V., and Midgley, P. M., Cambridge University Press, Cambridge, United Kingdom and New York, NY, USA, 659–740, 2013.
- 680 Olivier, J. G. J., Schure, K. M., and Peters, J. A. H. W.: Trends in global CO₂ emissions; 2017 Report, PBL Netherlands Environmental Assessment Agency, The Hague/Bilthoven500114022, 2017.
- 685 Prinn, R. G., Weiss, R. F., Arduini, J., Arnold, T., DeWitt, H. L., Fraser, P. J., Ganesan, A. L., Gasore, J., Harth, C. M., Hermansen, O., Kim, J., Krummel, P. B., Li, S., Loh, Z. M., Lunder, C. R., Maione, M., Manning, A. J., Miller, B. R., Mitrevski, B., Mühle, J., O'Doherty, S., Park, S., Reimann, S., Rigby, M., Saito, T., Salameh, P. K., Schmidt, R., Simmonds, P. G., Steele, L. P., Vollmer, M. K., Wang, R. H., Yao, B., Yokouchi, Y., Young, D., and Zhou, L.: History of Chemically and Radiatively Important Atmospheric Gases from the Advanced Global Atmospheric Gases Experiment (AGAGE), *Earth Syst. Sci. Data Discuss.*, 1-39, 10.5194/essd-2017-134, 2018.
- 695 Purohit, P., and Höglund-Isaksson, L.: Global emissions of fluorinated greenhouse gases 2005–2050 with abatement potentials and costs, *Atmos. Chem. Phys.*, 17, 2795–2816, 10.5194/acp-17-2795-2017, 2017.

- Raoux, S.: Implementing technologies for reducing PFC emissions, *Solid State Technology*, 50, 49-52, 2007.
- 700 Rigby, M., Prinn, R. G., O'Doherty, S., Miller, B. R., Ivy, D., Muhle, J., Harth, C. M., Salameh, P. K., Arnold, T., Weiss, R. F., Krummel, P. B., Steele, L. P., Fraser, P. J., Young, D., and Simmonds, P. G.: Recent and future trends in synthetic greenhouse gas radiative forcing, *Geophys. Res. Lett.*, 41, 2623-2630, 10.1002/2013gl059099, 2014a.
- 705 Rigby, M., Prinn, R. G., O'Doherty, S., Miller, B. R., Ivy, D., Mühle, J., Harth, C. M., Salameh, P. K., Arnold, T., Weiss, R. F., Krummel, P. B., Steele, L. P., Fraser, P. J., Young, D., and Simmonds, P. G.: Recent and future trends in synthetic greenhouse gas radiative forcing, *Geophys. Res. Lett.*, 41, 2623-2630, 10.1002/2013gl059099, 2014b.
- Ryall, D. B., and Maryon, R. H.: Validation of the UK Met. Office's name model against the ETEX dataset, *Atmos. Environ.*, 32, 4265-4276, 10.1016/s1352-2310(98)00177-0, 1998.
- 710 SEMI: SEMI® World Fab Forecast. SEMI (Ed.), http://www.semi.org/en/Store/MarketInformation/fabdatabase/ctr_027238, 2017.
- 715 Simmonds, P. G., Rigby, M., McCulloch, A., Vollmer, M. K., Henne, S., Mühle, J., O'Doherty, S., Manning, A. J., Krummel, P. B., Fraser, P. J., Young, D., Weiss, R. F., Salameh, P. K., Harth, C. M., Reimann, S., Trudinger, C. M., Steele, L. P., Wang, R. H. J., Ivy, D. J., Prinn, R. G., Mitrevski, B., and Etheridge, D. M.: Recent increases in the atmospheric growth rate and emissions of HFC-23 (CHF₃) and the link to HCFC-22 (CHClF₂) production, *Atmos. Chem. Phys.*, 18, 4153-4169, 10.5194/acp-18-4153-2018, 2018.
- 720 Stohl, A., Kim, J., Li, S., O'Doherty, S., Mühle, J., Salameh, P. K., Saito, T., Vollmer, M. K., Wan, D., Weiss, R. F., Yao, B., Yokouchi, Y., and Zhou, L. X.: Hydrochlorofluorocarbon and hydrofluorocarbon emissions in East Asia determined by inverse modeling, *Atmos. Chem. Phys.*, 10, 3545-3560, 2010.
- Thomson, D. J., Webster, H. N., and Cooke, M. C.: Developments in the Met Office InTEM volcanic ash source estimation system, Part 1: Concepts Met Office, 2017.
- 725 Totterdill, A., Kovács, T., Feng, W., Dhomse, S., Smith, C. J., Gómez-Martín, J. C., Chipperfield, M. P., Forster, P. M., and Plane, J. M. C.: Atmospheric lifetimes, infrared absorption spectra, radiative forcings and global warming potentials of NF₃ and CF₃CF₂Cl (CFC-115), *Atmos. Chem. Phys.*, 16, 11451-11463, 10.5194/acp-16-11451-2016, 2016.
- 730 Vogel, H., Flerus, B., Stoffner, F., and Friedrich, B.: Reducing Greenhouse Gas Emission from the Neodymium Oxide Electrolysis. Part I: Analysis of the Anodic Gas Formation, *Journal of Sustainable Metallurgy*, 3, 99-107, 10.1007/s40831-016-0086-0, 2017.
- Wangxing, L., Xiping, C., Shilin, Q., Baowei, Z., and Bayliss, C.: Reduction Strategies for PFC Emissions from Chinese Smelters, in: *Light Metals 2013*, edited by: Sadler, B. A., Springer International Publishing, Cham, 893-898, 2016.
- 735 Webster, H. N., Thomson, D. J., and Cooke, M. C.: Developments in the Met Office InTEM volcanic ash source estimation system, Part 2: Results, Met Office, 2017.

World Semiconductor Council: Joint Statement of the 21st Meeting of the World Semiconductor Council (WSC). Kyoto, Japan, 2017.

740 Yang, C.-F. O., Kam, S.-H., Liu, C.-H., Tzou, J., and Wang, J.-L.: Assessment of removal efficiency of perfluorocompounds (PFCs) in a semiconductor fabrication plant by gas chromatography, *Chemosphere*, 76, 1273-1277, 10.1016/j.chemosphere.2009.06.039, 2009.

745 Yao, B., Vollmer, M. K., Zhou, L. X., Henne, S., Reimann, S., Li, P. C., Wenger, A., and Hill, M.: In-situ measurements of atmospheric hydrofluorocarbons (HFCs) and perfluorocarbons (PFCs) at the Shangdianzi regional background station, China, *Atmos. Chem. Phys.*, 12, 10181-10193, 10.5194/acp-12-10181-2012, 2012.

Yokouchi, Y., Taguchi, S., Saito, T., Tohjima, Y., Tanimoto, H., and Mukai, H.: High frequency measurements of HFCs at a remote site in east Asia and their implications for Chinese emissions, *Geophys. Res. Lett.*, 33, n/a-n/a, 10.1029/2006GL026403, 2006.

750 Zhang, L., Wang, X., and Gong, B.: Perfluorocarbon emissions from electrolytic reduction of rare earth metals in fluoride/oxide system, *Atmospheric Pollution Research*, doi:10.1016/j.apr.2017.06.006., 2017.

Figures

755 Figure 1: An aggregation of the dilution matrices from 2013, generated using NAME output (see section 2.2), illustrating the relative sensitivity of measurements at GSN to emissions in the region.

760 Figure 2: Schematic of the domain ‘edges’ as applied in the inversion. 11 domain border conditions were estimated as depicted from 1 to 11 as a multiplying factor to the prior baseline estimated using data from the Mace Head observatory. Below 6 km the domain border was divided 8 times: NNE, ENE, ESE, SSE, SSW, WSW, WNW and NNW; between 6 to 9 km the domain border was just divided between north and south; and air arriving from above 9 km was considered from one ‘high’ domain border. Average posterior multiplying factors for CF₄ over the eight years were 1.00 ± 0.01 (NNE), 0.97 ± 0.06 (ENE), 1.02 ± 0.05 (ESE), 0.99 ± 0.01 (SSE), 1.00 ± 0.01 (SSW), 0.99 ± 0.01 (WSW), 1.00 ± 0.00 (WNW), 1.00 ± 0.01 (NNW), 1.00 ± 0.00 (6 to 9 km north), 1.00 ± 0.05 (6 to 9 km south), 0.97 ± 0.03 (above 9 km).

770 Figure 3: Time series of CF₄ measurements during 2013 – an example year with the most uninterrupted time series. Prior baseline (blue) is adjusted in the inversion using the baseline condition variables, producing a posterior baseline (red). During the summer months the proportion of air arriving from the south significantly rises causing a large shift in the posterior baseline relative to the prior baseline calculated from Mace Head data.

775 Figure 4: Time series of country emission totals 2008-2015. Annual inversion results are given for each gas for three different levels of uncertainty applied to the prior emission map: 100, 1000, and 10,000 times the emissions magnitude for each grid cell. The aggregated country totals from the prior dataset are also given.

780 Figure 5: The effect of the regridding routine on posterior emission distributions for CF₄. Maps A, C and E are posterior emissions maps at the initial inversion resolution, at 0 regridding steps, at 25 regridding steps and at 50 regridding steps, respectively. Maps B, D, F show the emissions magnitude minus the uncertainty calculated for each inversion grid box at the same regridding levels (0, 25, and 50), which demonstrates the relative uncertainty of the emissions distribution obtained for South Korea. Results are from inversions with initial uncertainty on the prior emissions field is set to 100 times emissions at each fine grid square. Units in Gg m⁻² yr⁻¹.

785 Figure 6: Emissions maps for all years of data available for CF₄. Results are from inversions with initial uncertainty on the prior emissions field is set to 100 times emissions at each fine grid square. Units in Gg m⁻² yr⁻¹. See Figure S7 for corresponding maps of emissions magnitude minus the uncertainty.

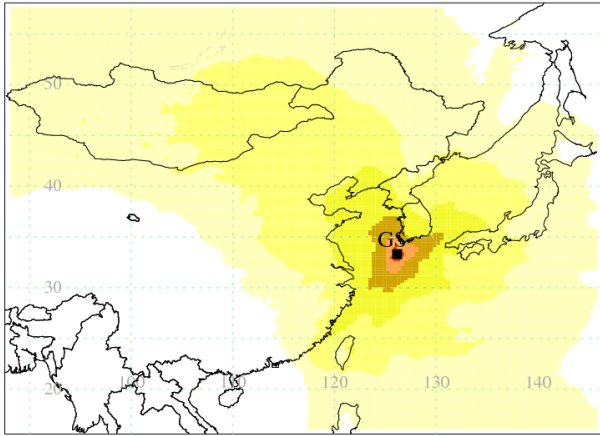
790 Figure 7: Emissions maps for both years of data available for NF₃: Maps A and C are posterior emissions maps for years 2014 and 2015, respectively. Maps B and D show the emissions magnitude minus the uncertainty calculated for each inversion grid box maps for years 2014 and 2015, respectively. Results are from inversions with initial uncertainty on the prior emissions field is set to 100 times emissions at each fine grid square. Units in Gg m⁻² yr⁻¹.

795 Figure 8: As for Figure 5 but for HFC-23

Tables

800 Table 1: Annual posterior emissions estimates for the five main emitting countries surrounding GSN (Gg yr^{-1}). These posterior emissions estimates are from the inversion that uses a prior emissions uncertainty on each fine grid cell of 100x the prior emission.

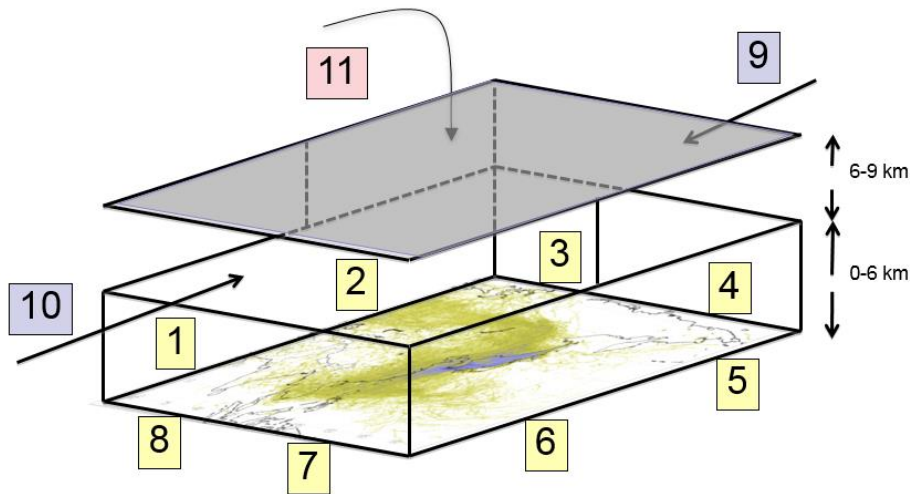
2013



Maximum value = 16.067 s/m

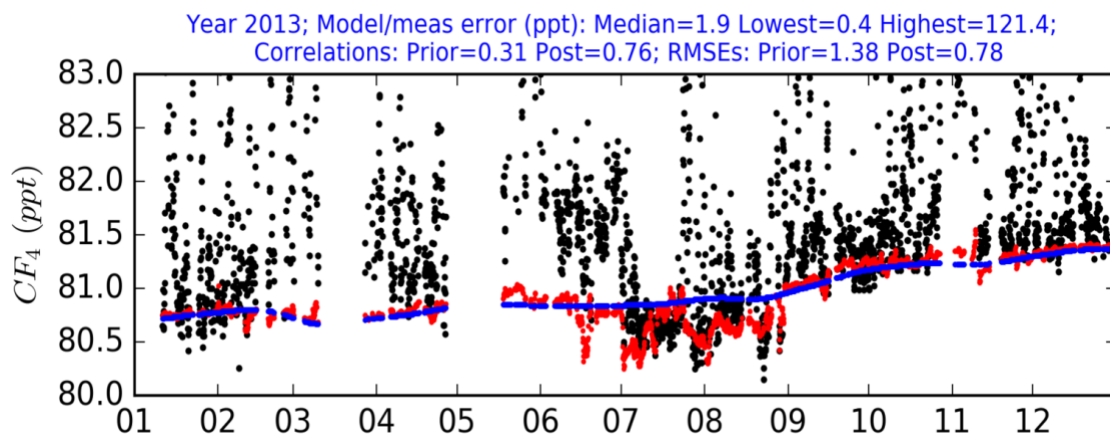
805 0.003 0.010 0.030 0.100 0.300 1.000 3.000 10.000 30.000

Figure 1



810 Figure 2

815



820 Figure 3

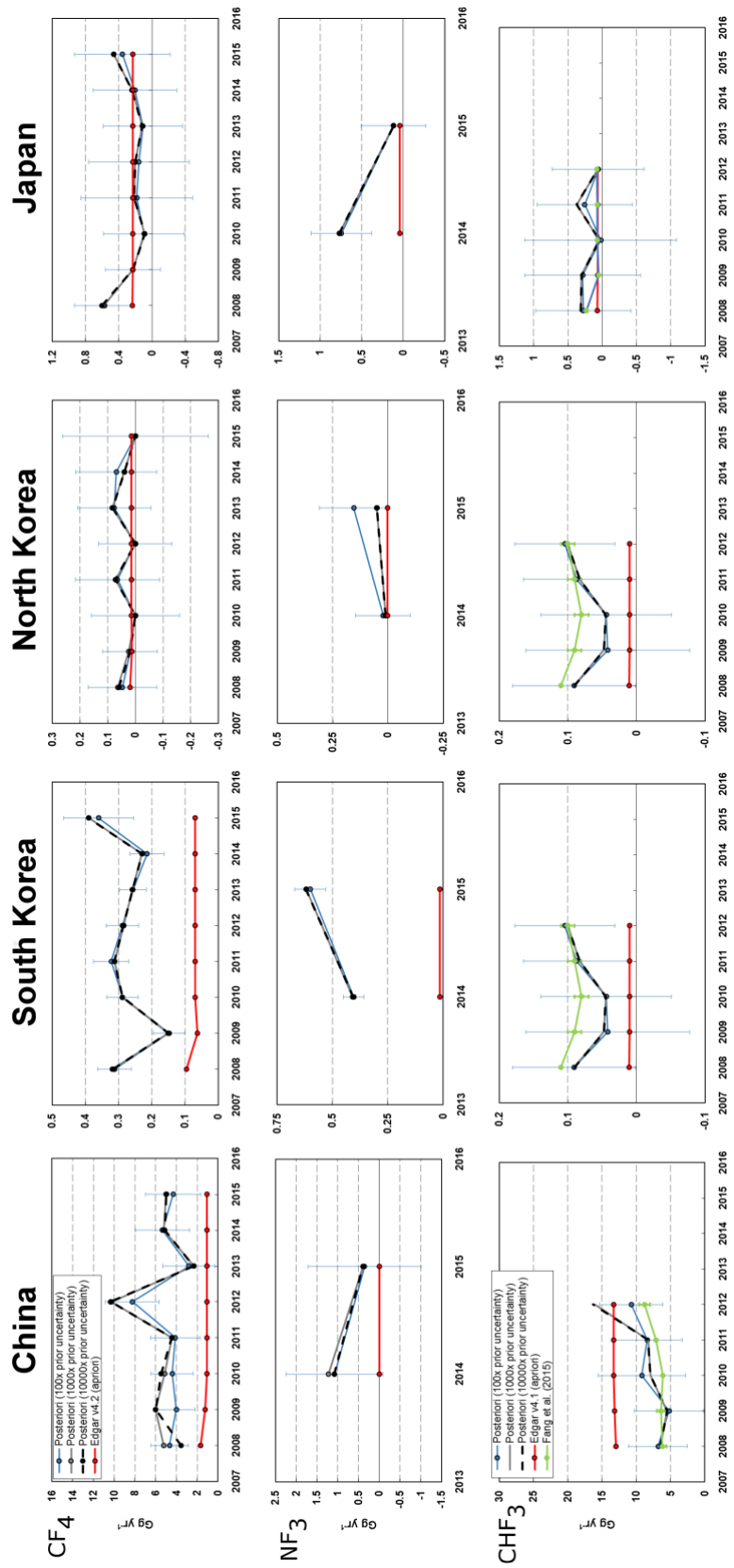


Figure 4

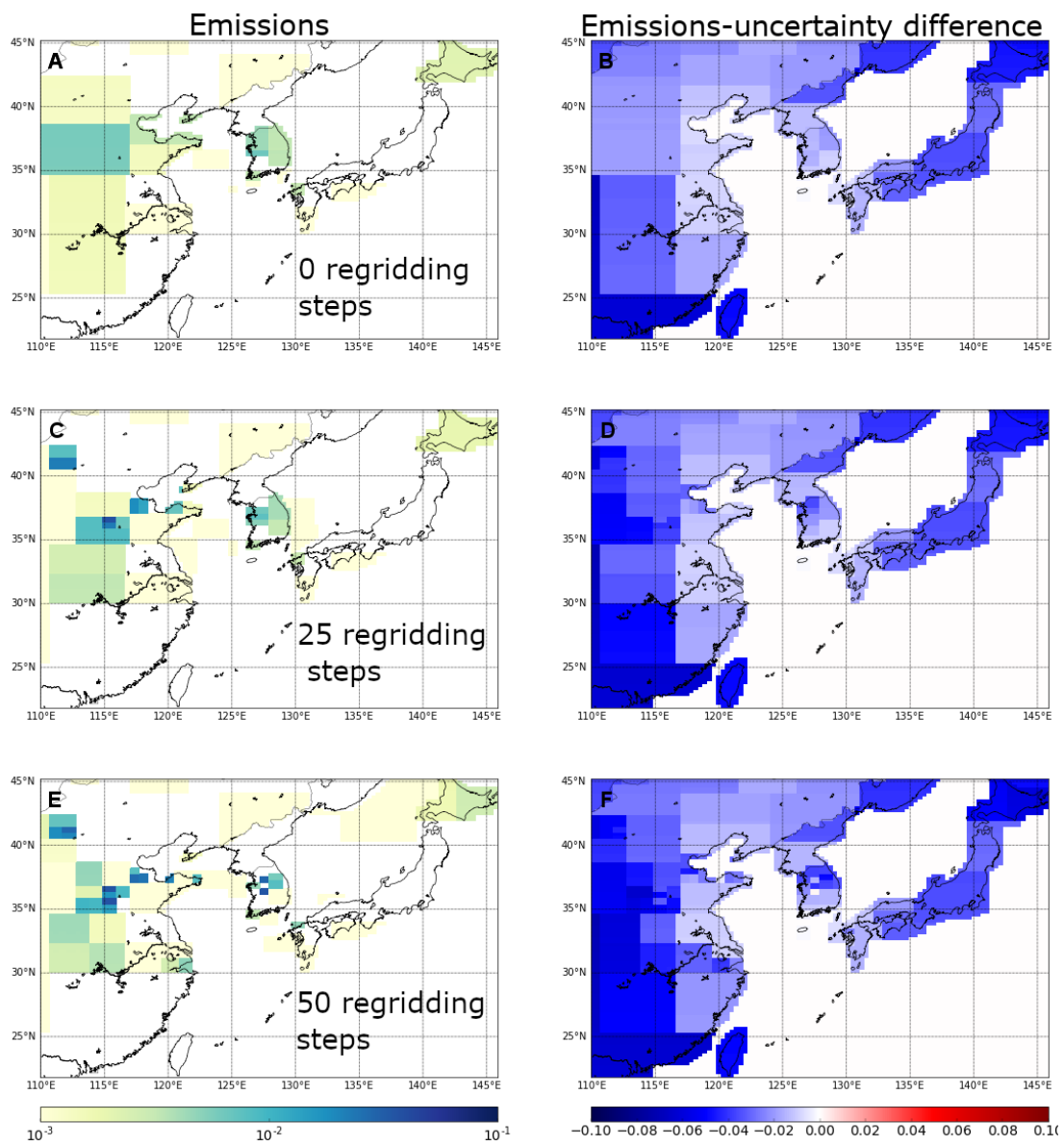
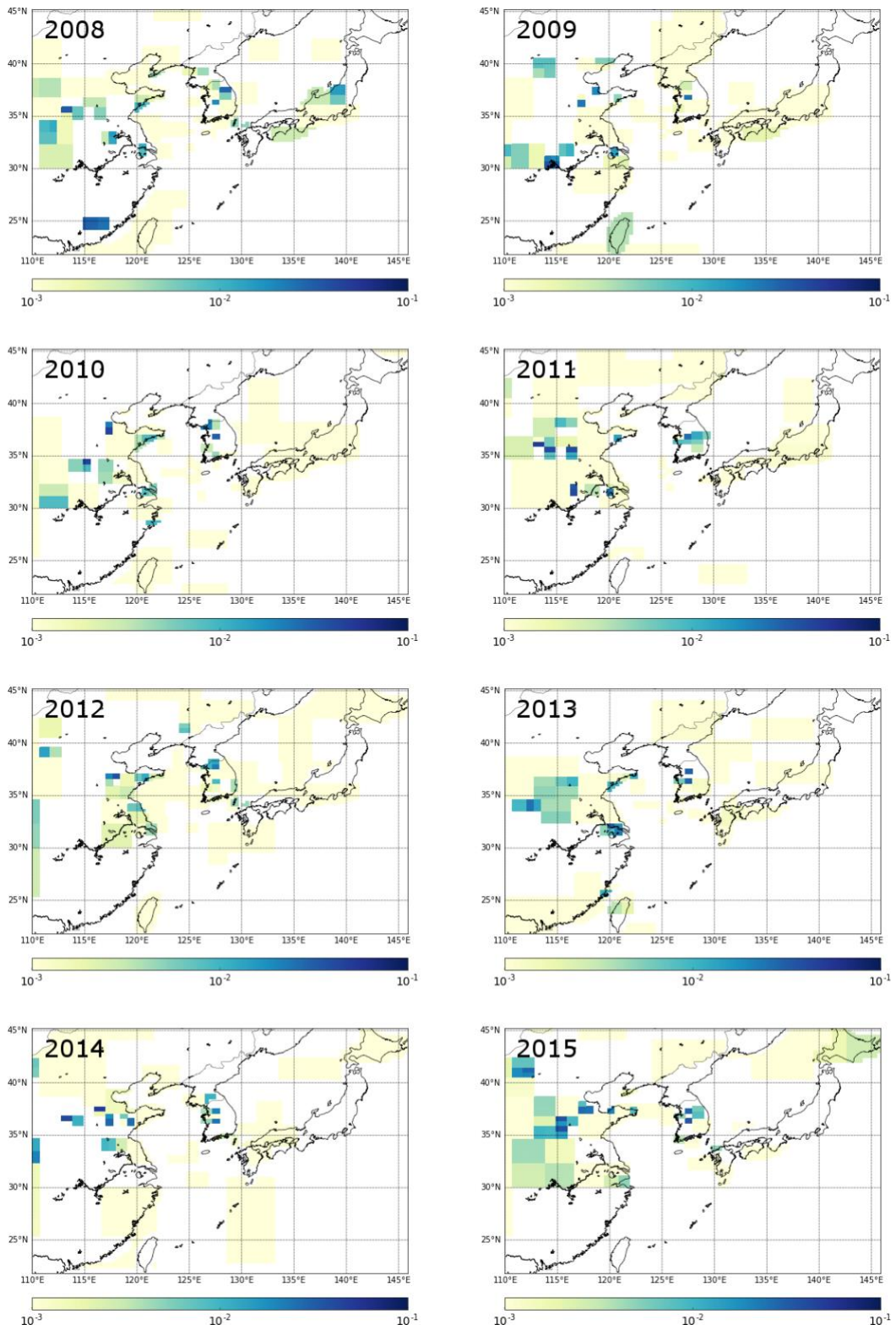


Figure 5



830

Figure 6

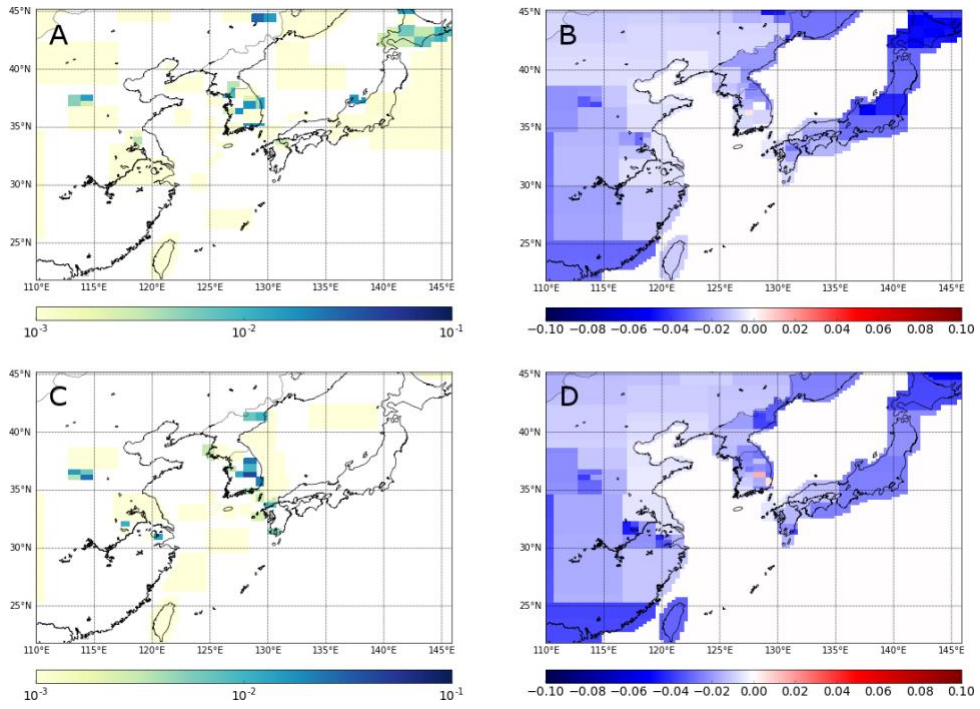


Figure: 7

835

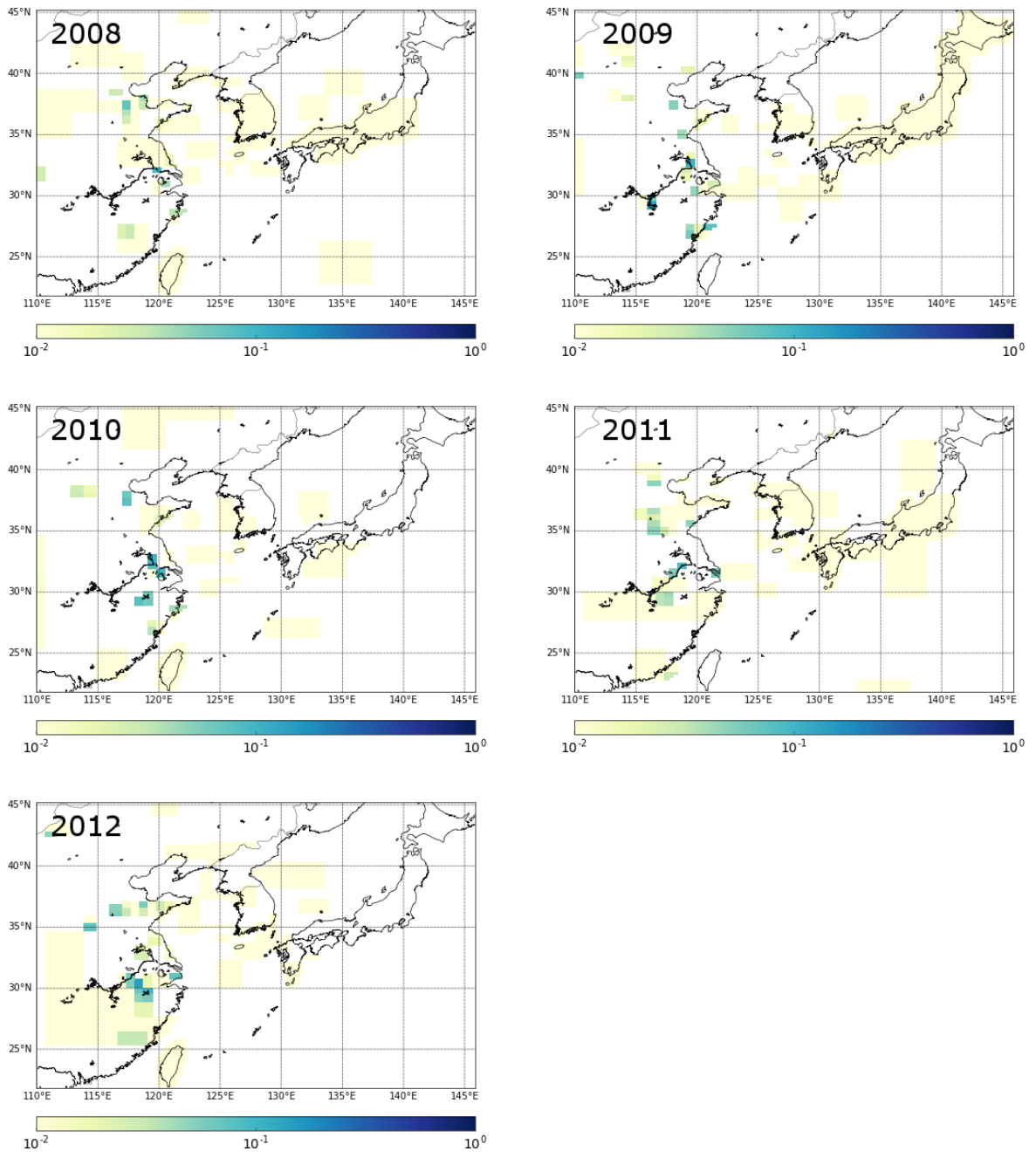


Figure 8

	CF ₄					NF ₃					HFC-23									
	China	S.Korea	N.Korea	Japan	Taiwan	China	S.Korea	N.Korea	Japan	Taiwan	China	S.Korea	N.Korea	Japan	Taiwan					
2008	4.66 (1.82) [#]	0.31 (0.05) [#]	0.05 (0.12) [#]	0.57 (0.36) [#]	0.01 (0.07)						6.8 (4.3)	0.09 (0.09)	0.08 (0.28)	0.28 (0.69)	0.11 (0.15)					
2009	4.01 (1.80)	0.15 (0.05)	0.02 (0.10)	0.23 (0.33)	0.32 (0.17)											5.2 (5.1)	0.04 (0.12)	0.00 (0.29)	0.29 (0.84)	0.00 (0.48)
2010	4.42 (2.06)	0.29 (0.05)	0.00 (0.16)	0.10 (0.48)	0.06 (0.13)											9.2 (6.4)	0.04 (0.10)	0.00 (0.39)	0.02 (1.11)	0.00 (0.31)
2011	4.12 (2.37)	0.32 (0.05)	0.06 (0.15)	0.18 (0.67)	0.00 (0.26)											8.4 (5.1)	0.09 (0.08)	0.00 (0.27)	0.26 (0.69)	0.00 (0.41)
2012	8.25 (2.59)	0.29 (0.05)	0.00 (0.13)	0.16 (0.60)	0.04 (0.40)											10.7 (4.6)	0.10 (0.07)	0.00 (0.23)	0.06 (0.67)	0.24 (0.46)
2013	2.82 (2.49)	0.26 (0.04)	0.08 (0.13)	0.11 (0.48)	0.09 (0.26)															
2014	5.35 (2.61)	0.21 (0.05)	0.07 (0.15)	0.21 (0.50)	0.00 (0.30)	1.08 (1.17)	0.40 (0.05)	0.02 (0.12)	0.75 (0.36)	0.03 (0.09)										
2015	4.33 (2.65)	0.36 (0.11)	0.00 (0.26)	0.36 (0.57)	0.00 (0.44)	0.36 (1.36)	0.60 (0.07)	0.15 (0.16)	0.11 (0.39)	0.00 (0.27)										

Kim et al. (2010) estimated CF₄ emissions from China in the range 1.7-3.1 Gg yr⁻¹ and Li et al. (2011) 1.4-2.9 Gg yr⁻¹. For South and North Korea (combined) Li et al. (2011) estimated emissions of CF₄ at 0.19-0.26 Gg yr⁻¹ and from Japan at 0.2-0.3 Gg yr⁻¹.

Table